

# Formation of Perfusion Defects in Lymph Nodes During the Early Stage of Metastasis

**Tepei Yamaki**

Tohoku University

**Ariunbuyan Sukhbaatar**

Tohoku University

**Ryohei Kikuchi**

Tohoku University

**Maya Sakamoto**

Tohoku University

**Shiro Mori**

Tohoku University

**Tetsuya Kodama** (✉ [kodama@tohoku.ac.jp](mailto:kodama@tohoku.ac.jp))

Tohoku University

---

## Research Article

**Keywords:** lymph node metastasis, mouse model, focal perfusion defect, CT, ultrasound, non-enlarged lymph node

**Posted Date:** January 23rd, 2021

**DOI:** <https://doi.org/10.21203/rs.3.rs-150367/v1>

**License:**   This work is licensed under a Creative Commons Attribution 4.0 International License.

[Read Full License](#)

---

# Abstract

A perfusion defect in metastatic lymph nodes (LNs) can be visualized as a localized area of low contrast on contrast-enhanced CT, MRI or ultrasound images. Hypotheses for perfusion defect include abnormal hemodynamics in neovascular vessels and decrease in blood flow in pre-existing blood vessels in the parenchyma due to compression of tumor growth in the LNs. However, the mechanism of perfusion defects in LNs during the early stage of LN metastasis has not yet been investigated. Here we show that the formation of a tumor mass with very few microvessels was associated with the development of a perfusion defect in the non-enlarged LN at the early stage of LN metastasis. We found in a mouse model of LN metastasis induced using non-keratinizing tumor cells that during formation of the perfusion defect in non-enlarged LN, the number of blood vessels  $\leq 50$   $\mu\text{m}$  in diameter decreased, while the volume of existing blood vessels  $>50$   $\mu\text{m}$  in diameter increased using contrast-enhanced high-frequency ultrasound and contrast-enhanced micro-CT imaging systems with a maximum spatial resolution of  $> 30$   $\mu\text{m}$ . Furthermore, we found that tumor angiogenesis and  $\text{pO}_2$  changes in the metastatic LN were not observed. Our results demonstrate that the perfusion defect appear to be a specific form of tumorigenesis in the LN as vascular-rich organ at the early stage of metastasis. We anticipate a perfusion defect on ultrasound, CT or MRI images to be used as an indicator in the non-enlarged LN at the early stage of LN metastasis.

## Introduction

Sentinel lymph nodes (LNs) receive lymphatic drainage from the primary tumor and are the organs at highest risk of metastasis<sup>1</sup>. The presence or absence of LN metastasis is highly relevant to cancer staging, patient prognosis, treatment planning (including surgery, radiotherapy and adjuvant chemotherapy), and the risks of local tumor recurrence and cancer-specific mortality<sup>2</sup>. Recent experiments in mice have indicated that tumor cells in afferent lymphatic vessels can invade the subcapsular sinus and infiltrate the veins running over the LN, thereby metastasizing to distant organs via hematogenous routes at the early stage of metastasis<sup>3-5</sup>. Therefore, early diagnosis and treatment of metastatic lymph node at the early stage of metastasis<sup>6,7</sup> are essential to prevent distant metastasis<sup>8</sup>. Although the diagnosis of LN metastasis has been improved by the use of multiple biomarkers<sup>9,10</sup>, there are no perfect prognostic markers that can reliably predict cancer recurrence<sup>11</sup>. Diagnostic modalities such as CT, MRI and ultrasound cannot detect the pathological changes associated with LN metastasis, and their diagnostic accuracy is generally lower for smaller LNs<sup>1</sup>.

A perfusion defect in LNs can be visualized as a localized area of low contrast on contrast-enhanced CT, MRI or ultrasound images. Perfusion defects have been identified in many types of tumor cells<sup>12,13</sup>. The reported incidence of perfusion defects correlates with LN size, being 10–33% for metastatic LNs  $< 10$  mm in diameter and 56–63% for metastatic LNs  $> 15$  mm in diameter<sup>14</sup>. Measurement of the difference between the maximum and minimum signal intensity values on contrast-enhanced ultrasound images can be used to evaluate perfusion defects and to detect early LN metastasis in clinically node-negative

breast cancer<sup>15-17</sup>. Central necrosis is an important feature used to diagnose small metastatic LNs, especially those that do not match the diagnostic criterion for size. The term 'central necrosis' is a synonym for a perfusion defect and is often used to refer to actual necrosis, the replacement of part of the LN parenchyma by tumor cells, or both. Since the mechanism of LN metastasis involves the proliferation of tumor cells that invade the subcapsular sinus from afferent lymphatic vessels, 'perfusion defect' is a more appropriate term than 'central necrosis.' Hypotheses for perfusion defect are an increase in the intranodal pressure due to tumor growth which compresses the pre-existing blood vessels in the parenchyma, as well as abnormal hemodynamics in neovascular vessels and hypoxia generated by angiogenesis during rapid tumor growth. Perfusion defect is observed even in metastatic LNs of well-differentiated squamous epithelial cancer cells due to keratinization<sup>18</sup>. However, although tumor growth in the non-enlarged LN increases the internal pressure<sup>19</sup>, it does not induce neovascularization<sup>20,21</sup> because the LN already has a rich vascular network<sup>3,13,22-24</sup>. In addition, lymphangiography revealed decrease in the lymphatic sinus region due to the tumor formation at the early stage of metastasis, i.e., the parenchyma was replaced with tumor cells<sup>25</sup>. Therefore, a perfusion defect in a metastatic LN at an early stage is presumed to be an event that is distinct from those associated with hypoxia, angiogenesis, keratinization and tissue necrosis, which occur as tumor growth rapidly progresses<sup>26,27</sup>. The present study aims to elucidate the mechanisms of perfusion defect formation in the tumor mass in the non-enlarged LN at the early stage of metastasis.

## Results

Metastasis in the PALN was detected from day 7 after KM-Luc/GFP cell inoculation into the SiLN and from day 14 after FM3A-Luc cell inoculation (**Fig. 1a, b**). Luciferase activity in both the SiLN and PALN increased with time (Fig. 1a, b). Luciferase activity was higher in the SiLN (inoculation site) than in the PALN (metastatic site) after inoculation. FM3A-Luc-inoculated solid tumors exhibited continuous growth (**Fig. 1S**) that was similar to that reported for FM3A-Luc-inoculated solid tumors<sup>19,20</sup>. First, we compared the  $pO_2$  between metastatic PALN, solid tumor, control SiLN, control PALN, tumor-inoculated SiLN and tail vein. The interior of the solid tumor became hypoxic and exhibited a significant decrease in  $pO_2$  as it grew. By contrast, the  $pO_2$  in the LNs remained constant irrespective of whether they contained tumor (**Fig. 1c**; one-way ANOVA and Tukey's post-hoc test:  $P < 0.05$ , solid tumor vs metastatic PALN;  $P < 0.01$ , solid tumor vs tumor-inoculated SiLN; and  $P < 0.01$ , solid tumor vs tail vein).

Contrast-enhanced high-frequency ultrasound imaging was used to examine the volumetric and vascular changes in the PALN at different times after KM-Luc/GFP cell and FM3A-Luc cell inoculation (**Fig. 2**). Heat maps of the vessels in the PALN (**Fig. 2a**) did not show a perfusion defect at day 0 but did reveal a perfusion defect that lacked contrast agent (arrow) at day 10 after KM-Luc/GFP cell inoculation. Similarly, a perfusion defect (arrow) was observed on day 21 after FM3A-Luc cell inoculation, and the size of the defect expanded with time (days 28 and 35; **Fig. 2a**). **Figure 2b** shows data for the normalized vascular area ratio and normalized LN volume. There were no significant changes in LN volume up to day 10 following KM-Luc/GFP cell inoculation and up to day 35 following FM3A-Luc cell inoculation.

Therefore, these LNs can be considered to be non-enlarged LNs based on the ultrasonography findings. There were also no significant changes in the vascular area ratio. However, this parameter showed a slight tendency to increase after KM-Luc/GFP cell inoculation and decrease following FM3A-Luc cell inoculation.

Next, contrast-enhanced micro-CT imaging was used to observe the vascular structure of the PALN (**Fig. 3**). Mice were perfused sequentially with PBS, 4% paraformaldehyde and gelatin-based barium contrast agent on days 4, 7 and 10 after KM-Luc/GFP cell inoculation and on days 14, 21, 28 and 35 after FM3A-Luc cell inoculation, and the PALNs were excised 2 h after cooling and then imaged. In the control group (day 0, no tumor cell inoculation), the LN was shaped like a flat oval (**Fig. 3a, b**), and one side of its surface was covered with dense blood vessels, including the thoracoepigastric vein (TEV). In contrast, the reverse side had far fewer blood vessels. The arrows in **Fig. 3** indicate the TEV anastomosed to many intranodal blood vessels (**Video S1**). The blood in the TEV flows from the PALN to the subclavian vein<sup>4,5</sup>. Perfusion defects (arrowheads) were observed following KM-Luc/GFP cell inoculation (**Video S2**) and FM3A-Luc cell inoculation (**Video S3**).

The volume of the PALN and the volume of its internal vessels were calculated from 3D contrast-enhanced micro-CT images (**Fig. 4**). There were no significant changes in PALN volume over time following the inoculation of KM-Luc/GFP cells or FM3A-Luc cells (i.e., the PALN can be considered a non-enlarged LN), in agreement with the data shown in **Fig. 2**. Vessel volume increased after KM-Luc/GFP cell inoculation (one-way ANOVA:  $P < 0.05$ , day 0 vs day 7;  $P < 0.01$ , day 0 vs day 10) and FM3A-Luc cell inoculation (one-way ANOVA:  $P < 0.05$ , day 0 vs day 21;  $P < 0.01$ , day 0 vs day 28) (**Fig. 4a**). Total blood vessel length in the PALN, calculated from the CT images, showed no changes in both tumor cell groups (**Fig. 4b**).

**Figure 4c, d** shows the distribution of blood vessel diameter in the PALN after tumor cell inoculation into the SiLN. Blood vessels with a diameter  $< 50 \mu\text{m}$  accounted for 80% of all blood vessels before the inoculation of both tumor cell types into the SiLN (day 0; **Fig. 4c, d**). However, following the inoculation of KM-Luc/GFP cells (**Fig. 4c**), the number of blood vessels with a diameter  $< 50 \mu\text{m}$  decreased (one-way ANOVA:  $P < 0.000$ , day 0 vs day 4;  $P < 0.000$ , day 0 vs day 7;  $P < 0.000$ , day 0 vs day 10;  $P < 0.01$ , day 4 vs day 7;  $P < 0.01$  day 4 vs day 10;  $P < 0.05$ , day 7 vs day 10) and the number of blood vessels with a diameter  $> 50 \mu\text{m}$  increased as tumor growth progressed. The above findings are consistent with the dilation of existing blood vessels. After the inoculation of FM3A-Luc cells (**Fig. 4d**), the number of blood vessels with a diameter  $< 50 \mu\text{m}$  decreased (one-way ANOVA:  $P < 0.000$ , day 0 vs day 10;  $P < 0.01$ , day 4 vs day 7;  $P < 0.001$ , day 4 vs day 10;  $P < 0.01$ , day 7 vs day 10), and those with a diameter  $> 50 \mu\text{m}$  showed increases over time as the tumor grew.

**Figure 5** shows PALN tissue sections obtained after CT imaging. KM-Luc/GFP cells formed a tumor mass in the LN and proliferated expansively, but the boundary with surrounding normal tissue was well defined. There were no mature blood vessels containing blood in the tumor mass. However, blood vessels around the tumor mass appeared compressed, and some dilated blood vessels were also seen (**Fig. 5a**). FM3A-

Luc cells proliferated invasively in the PALN, resulting in a poorly defined boundary with surrounding normal tissue. No mature blood vessels were evident in the tumor tissue. Some tumor cells had infiltrated the surrounding tissue's blood vessels to destroy the vasculature at the invasion site, and no dilated blood vessels were found in the tissue surrounding the tumor (**Fig. 5a**). **Figure 5b** shows the CD31-positive vascular density calculated from histological images (one-way ANOVA, KM-Luc/GFP group:  $P < 0.05$ , day 0 vs day 10; one-way ANOVA, FM3A-Luc group:  $P < 0.01$ , day 0 vs day 28) and the vascular density calculated from CT images (one-way ANOVA, KM-Luc/GFP group:  $P < 0.01$ , day 0 vs day 4;  $P < 0.01$ , day 0 vs day 7;  $P < 0.01$ , day 0 vs day 10; one-way ANOVA, FM3A-Luc group:  $P < 0.01$ , day 0 vs day 28). Vascular density increased with time, indicating that the perfusion defect was formed in a microenvironment in which no tumor angiogenesis was induced and the existing blood vessels were dilated.

## Discussion

In the present study, we used contrast-enhanced high-frequency ultrasound and contrast-enhanced *ex vivo* micro-CT imaging to examine the processes by which perfusion defects are formed in non-enlarged LNs after inoculation with two different types of non-keratinizing tumor cells. The blood vessel network is well developed in normal LNs and provides an adequate supply of oxygen and nutrients (day 0 in **Fig. 2a**, **Fig. 3a**)<sup>3,13,23,24</sup>. Formation of the perfusion defect was associated with the development of a tumor mass in a microenvironment that exhibited loss of vessels  $\leq 50$   $\mu\text{m}$  in diameter and dilation of existing blood vessels  $> 50$   $\mu\text{m}$  in diameter, where the spatial resolution was  $> 30$   $\mu\text{m}$ . During the formation of the perfusion defect, LN volume did not change (**Fig. 2b**, **Fig. 4a**), and tumor angiogenesis was not induced (**Fig. 4**, **Fig. 5**). We consider the dilated blood vessels to be primarily congested venous vessels that become dilated because the tumor causes a circulatory disturbance within the LN. The  $p\text{O}_2$  in the LN at the onset of perfusion defect development was the same as that in normal LNs (**Fig. 1c**).

Micro-CT-detectable perfusion defects are difficult to visualize with clinical CT and ultrasound modalities, which have a lower spatial and tissue resolution. Therefore, non-enlarged LNs would be diagnosed as clinical N0 (cN0) LNs even though they contained metastasized tumor cells. Additionally, non-enlarged LNs would not be considered to be in the early stage of metastasis from a histopathological standpoint because tumor cells have already grown out of the subcapsular sinus at this stage. Perfusion defects have been observed in metastatic LNs using clinical imaging modalities such as CT and ultrasonography and discussed the mechanisms of their formation with regard to cell type<sup>12</sup>, reactive LNs<sup>28</sup>, the fatty hilum<sup>29</sup>, tissue necrosis<sup>26,27</sup>, abnormal lymphatic drainage, keratinization<sup>30</sup> and biomarkers<sup>31,32</sup>. Importantly, perfusion defects in LNs were observed with each imaging modality, and the LNs were subjected to pathological analyses to determine whether they were cN0 or N1. The present finding was that in the early stage of metastasis, tumor cells replace microvascular areas to form a perfusion defect that is not pathologically necrotic tissue. During perfusion defect formation, replacement of parenchyma with tumor supplied by only a few microvessels occurs, intranodal pressure increased<sup>19</sup>,  $p\text{O}_2$  remained constant and tumor neovascularization was not induced<sup>20</sup>. Perfusion defects, which are formed by the

replacement of LN parenchyma with tumor cells, have also been observed with intranodal lymphangiography in non-enlarged LNs<sup>25</sup>. The characteristics of perfusion defect formation in LNs may explain why metastatic LNs show an inadequate response to hematologic systemic chemotherapy using small-molecule and macromolecular anticancer agents<sup>33,34</sup>.

The concept of LN-mediated hematogenous metastasis implies that tumor cells spread from metastatic LNs to distant vital organs via blood vessels. Our group has recently developed a lymphatic drug delivery system (LDDS) that aims to treat sentinel LNs and their downstream LNs by injecting anticancer drugs directly into the sentinel LNs<sup>8,35,36</sup>. This therapeutic system can treat metastatic LNs using smaller doses of anticancer drug than is required for systemic chemotherapy. Enhancing the sensitivity of clinical imaging modalities to detect perfusion defects in LNs will facilitate the identification of metastatic LNs that could be targeted with the LDDS, thereby substantially improving the quality of life of patients with cancer.

### **Implications for patient care**

Expanding the roles of contrast-enhanced CT, ultrasound or MRI to the imaging of perfusion defects in LNs could improve the monitoring of early-stage LN metastasis and facilitate cancer management. New drug delivery systems could be developed to target the tumor foci that form perfusion defects, considering that there are many discrepancies in the rate of tumor growth, the microenvironment and the blood composition in human and mouse tumor tissues.

## **Materials And Methods**

Experiments were carried out under established guidelines and approved by the Institutional Animal Care and Use Committee of Tohoku University. This study complies with ARRIVE guidelines for reporting animal experiment<sup>37</sup>.

### **Mice**

MXH10/*Mo-lpr/lpr* (MXH10/*Mo/lpr*) mice (13–16 weeks of age) were used in the experiments<sup>38</sup>. The mice develop enlarged LNs that reach up to 10 mm in diameter at 2.5–3 months of age, and the size and onset time of the LN swelling are stable and predictable. Mice were bred under specific pathogen-free conditions in the Animal Research Institute, Graduate School of Medicine, Tohoku University. Mice were housed in groups of four or fewer.

### **Cell lines**

Keratinizing tumor cells have been detected in LNs<sup>18</sup>. Therefore, we used two types of non-keratinizing tumor cells to eliminate the effect of keratinization in the present study: malignant fibrous histiocytoma-like (KM-Luc/GFP) cells, which express a fusion of the luciferase and enhanced green fluorescent protein genes, and C3H/He mouse mammary carcinoma (FM3A-Luc) cells, which express the luciferase gene<sup>38</sup>.

Cell lines were incubated (37°C, 5% CO<sub>2</sub>/95% air) until 80% confluence was achieved. Cell growth rate was 3.8/day for KM-Luc/GFP and 1.1/day for FM3A-Luc cells. Lack of *Mycoplasma* contamination was confirmed on the inoculation day (MycoAlert *Mycoplasma* Detection Kit; Lonza Rockland, Allendale, NJ, US).

### **Creation of solid tumor**

1.0 × 10<sup>6</sup> FM3A-Luc cells in 60 µL vehicle (20 µL of phosphate-buffered saline [PBS] plus 40 µL of 400 mg/mL Matrigel; Collaborative Biomedical Products, Bedford, MA, US) were injected into the right flanks of mice anesthetized with 2% isoflurane in oxygen (Abbott, Lake Forest, IL, US).

### **Mouse model of LN metastasis**

1.0 × 10<sup>4</sup> KM-Luc/GFP or 1.0 × 10<sup>4</sup> FM3A-Luc cells in 60 µL of a vehicle (20 µL of PBS plus 40 µL of 400 mg/mL Matrigel) were injected into the right subiliac LNs (SiLN) of mice anesthetized with 2% isoflurane in oxygen to induce metastasis in the right proper axillary lymph node (PALN) via lymphatic vessels<sup>6,7</sup>. In controls, 60 µL of the vehicle was injected into the SiLN. Inoculation (24-gauge needle) was guided by high-frequency ultrasound system (VEVO770; FUJIFILM VisualSonics, Tokyo, Japan) using a central frequency of 25-MHz transducer (RMV-710B, axial resolution 70 µm, FUJIFILM VisualSonics). The inoculation day was defined as day 0. Three groups were used to evaluate tumor growth/metastasis: control, KM-Luc/GFP and FM3A-Luc<sup>19</sup>. Metastasis to the PALN was assessed using *in vivo* bioluminescence imaging (IVIS; PerkinElmer, Waltham, MA, US) on days 0, 4, 7 and 10 for KM-Luc/GFP cells and days 0, 14, 21, 28 and 35 for FM3A-Luc cells. Metastasis was considered successful when PALN luciferase activity exceeded the background level in controls (~4 × 10<sup>4</sup> photons/sec). Data were normalized to the values on day 0 for KM-Luc/GFP cells and day 21 for FM3A-Luc cells.

### **Contrast-enhanced high-frequency ultrasound imaging with spatiotemporal analysis of pixel intensity variation**

A contrast-enhanced high-frequency ultrasound system (VEVO770; FUJIFILM VisualSonics) with a central frequency of 30-MHz transducer (RMV-708B, axial resolution 30 mm, FUJIFILM VisualSonics) was used to acquire two-dimensional (2D) images of the microvasculature within the PALN on days 0, 4, 7, and 10 post-inoculation of KM-Luc/GFP cells (*n* = 6) or days 21, 28 and 35 post-inoculation of FM3A-Luc cells (*n* = 10). Data were normalized to the values on day 0 for KM-Luc/GFP cells and day 21 for FM3A-Luc cells. Each transducer was fixed to a three-dimensional (3D) stage control system (Marsk-204-MS; Sigma Koki, Tokyo, Japan). Mice were placed in a lateral position on the heated stage after inhalation of 2% isoflurane in oxygen. The scanning distances were 20 mm for the PALN and 15 mm for the SiLN and field of view was 12 × 12 mm. The LNs were scanned in 100-mm-thick slices before and 60 sec after the administration of 100 µL of microbubbles (15 mg/mL, Sonazoid, Daiichi Sankyo) into the tail vein. The intranodal vascular network with vessel diameters <sup>3</sup> 30 mm only was analyzed due to spatial resolution. The mouse was anesthetized by administering 2% isoflurane in oxygen and rested on a heated stage

throughout the imaging session<sup>6,7</sup>. The images were analyzed by ultrasound contrast agent detection (UCAD) software<sup>39</sup> to detect temporal changes in the density of microvessels in the PALN.

### **Measurement of oxygen partial pressure (pO<sub>2</sub>)**

The pO<sub>2</sub> values of solid tumor ( $n = 2$ ), control (tumor-free) SiLN ( $n = 14$ ), control (tumor-free) PALN ( $n = 14$ ), tumor-inoculated SiLN ( $n = 7$ ), metastatic PALN ( $n = 7$ ) and tumor-free tail vein ( $n = 7$ ) were measured. The pO<sub>2</sub> values in the tumor-inoculated SiLN and metastatic PALN were measured when the luciferase activity of the PALN exceeded  $1.0 \times 10^6$  photons/sec. The mice were anesthetized with 2% isoflurane in oxygen and placed on a heated stage. The skin was incised to expose the target tissue, and a digital pO<sub>2</sub> monitor (Unique Medical Co., Ltd., Tokyo, Japan) was used to measure the pO<sub>2</sub>. A 24G indwelling needle (Terumo, Tokyo, Japan) was inserted into the center of the target tissue and then withdrawn, and a pO<sub>2</sub> monitor electrode (UOE-04T, Unique Medical Co., Ltd., Tokyo, Japan) was subsequently inserted. Values were recorded 3 min after electrode insertion using a data acquisition system (ML826 PowerLab 2/26, BioResearch Center, Aichi, Japan) and LabChart software (BioResearch Center).

### **Contrast-enhanced *ex vivo* micro-CT imaging**

*Ex vivo* contrast-enhanced imaging was performed using a micro-CT scanner specifically developed to image small laboratory animals (scanXmate/E090, Comscantecno Co., Kanagawa, Japan)<sup>25</sup>. A gelatin-based barium contrast agent (nontoxic due to its insolubility;  $1.0 \pm 0.3$  mm in size) was prepared as previously described<sup>40</sup>. Briefly, the left ventricle of the heart was perfused first with PBS to remove the blood and then with 4% paraformaldehyde (FUJIFILM Wako Pure Chemical Co., Osaka, Japan) to fix the tissues. Pre-heated gelatin-based barium contrast agent was injected to better visualize blood vessel branches including small capillaries. Mice were refrigerated (4°C) for at least 2 h after perfusion to solidify the gelatin-based contrast agent and prevent wash-out during fixation. PALNs were harvested and scanned at resolutions of 8 - 20  $\mu\text{m}$  for plain angiography and a slice thickness of 100  $\mu\text{m}$  for CT. Acquired slice data were rendered as 3D images (Amira, Maxnet Co., Ltd, Tokyo, Japan). Samples were obtained on day 4 ( $n = 5$ ), day 7 ( $n = 6$ ) and day 10 ( $n = 5$ ) for the KM-Luc/GFP group and on day 0 ( $n = 6$ ), day 14 ( $n = 5$ ), day 21 ( $n = 6$ ) and day 28 ( $n = 5$ ) for the FM3A-Luc group. The PALNs resected on each of these days were then used for histological analyses.

### **Histological analysis**

Some LNs were fixed overnight in 10% formalin at 4°C, dehydrated, embedded in paraffin, serially sectioned (3–5  $\mu\text{m}$ ), and either stained with hematoxylin and eosin (HE) or immunostained for CD31-positive cells. Histological images were captured using a digital camera (DP72; Olympus). To measure vessel density in each section, the 5 most vascularized fields (hotspot areas) were manually selected under low magnification ( $\times 40$  or  $\times 100$ ) by different researchers to avoid technical problems, and the percentage of each field stained for CD31 ( $\times 200$ ) was calculated using ImageJ software (National

Institutes of Health, Bethesda, MD, US). This hotspot selection process may have lacked reproducibility, so the selected areas represented high vascularized regions and different tumor localizations.

### **Statistical analysis**

Data are presented as the mean  $\pm$  S.E.M. Differences between groups were determined by one-way or two-way ANOVA followed by Tukey's post-hoc test.  $P < 0.05$  was considered statistically significant.

## **Abbreviations**

2D = two-dimensional

3D = three-dimensional

HE = hematoxylin and eosin

LDDS = lymphatic drug delivery system

LN = lymph node

MXH10/Mo/lpr = MXH10/Mo-*lpr/lpr*

pO<sub>2</sub> = partial pressure of oxygen

PALN = proper axillary lymph node

SiLN = subiliac lymph node

TEV = thoracoepigastric vein

UCAD = ultrasound contrast agent detection

## **Declarations**

### **Acknowledgments**

The authors would like to thank T. Sato for technical assistance and the Biomedical Research Core of Tohoku University Graduate School of Medicine for technical support. The study was supported by KAKENHI grants from the Japan Society for the Promotion of Science (20K20161 to SA; 18H03544 to SM; and 18H03544, 19K22941 and 20H00655 to KT).

### **Contributions**

Guarantors of the integrity of the entire study, K.T.; study concepts/study design or data acquisition or data analysis/interpretation, all authors; manuscript drafting or manuscript revision for important

intellectual content, all authors; approval of the final version of the submitted manuscript, all authors; agrees to ensure any questions related to the work are appropriately resolved, all authors; literature research, K.T., S.H.; statistical analysis, Y.T., A. S., K.T.; and manuscript editing, all authors.

### **Competing financial interest statement**

The authors declare no competing interests.

### **Data availability**

The data that support the findings of this study are available from the corresponding author upon reasonable request.

## **References**

- 1 van den Brekel, M. W. *et al.* Cervical lymph node metastasis: assessment of radiologic criteria. *Radiology***177**, 379-384 (1990).
- 2 Giuliano, A. E. *et al.* Locoregional recurrence after sentinel lymph node dissection with or without axillary dissection in patients with sentinel lymph node metastases: the American College of Surgeons Oncology Group Z0011 randomized trial. *Ann Surg***252**, 426-432 (2010).
- 3 Kodama, T., Mori, S. & Nose, M. Tumor cell invasion from the marginal sinus into extranodal veins during early-stage lymph node metastasis can be a starting point for hematogenous metastasis. *J Cancer Metastasis Treat***4**, 56 (2018).
- 4 Takeda, K., Mori, S. & Kodama, T. Study of fluid dynamics reveals direct communications between lymphatic vessels and venous blood vessels at lymph nodes of mice. *J Immunol Methods***445**, 1-9 (2017).
- 5 Shao, L., Takeda, K., Kato, S., Mori, S. & Kodama, T. Communication between lymphatic and venous systems in mice. *J Immunol Methods***424**, 100-105 (2015).
- 6 Li, L. *et al.* Enhanced Sonographic Imaging to Diagnose Lymph Node Metastasis: Importance of Blood Vessel Volume and Density. *Cancer Res***73**, 2082-2092 (2013).
- 7 Li, L., Mori, S., Sakamoto, M., Takahashi, S. & Kodama, T. Mouse model of lymph node metastasis via afferent lymphatic vessels for development of imaging modalities. *PloS one***8**, e55797 (2013).
- 8 Kodama, T., Matsuki, D., Tada, A., Takeda, K. & Mori, S. New concept for the prevention and treatment of metastatic lymph nodes using chemotherapy administered via the lymphatic network. *Sci Rep***6**, 32506 (2016).

- 9 Abe, M. *et al.* Highly sensitive detection of sentinel lymph node metastasis of breast cancer by digital PCR for RASSF1A methylation. *Oncol Rep***42**, 2382-2389 (2019).
- 10 Oka, R. *et al.* Annexin A8 is a novel molecular marker for detecting lymph node metastasis in oral squamous cell carcinoma. *Oncotarget***7**, 4882-4889 (2016).
- 11 Ruiz, E. M. L. *et al.* A novel gene panel for prediction of lymph-node metastasis and recurrence in patients with thyroid cancer. *Surgery***167**, 73-79 (2020).
- 12 Ohta, T., Nishioka, M., Nakata, N., Fukuda, K. & Kato, K. Five cases of axillary lymph node metastatic breast cancer on contrast-enhanced sonography. *J Ultrasound Med* **34**, 1131-1137 (2015).
- 13 Rubaltelli, L. *et al.* Evaluation of lymph node perfusion using continuous mode harmonic ultrasonography with a second-generation contrast agent. *J Ultrasound Med* **23**, 829-836 (2004).
- 14 Nakamura, T. & Sumi, M. Nodal imaging in the neck: recent advances in US, CT and MR imaging of metastatic nodes. *Eur Radio***17**, 1235-1241, doi:10.1007/s00330-006-0490-0 (2007).
- 15 Mori, N. *et al.* Perfusion contrast-enhanced ultrasound to predict early lymph-node metastasis in breast cancer. *Jpn J Radio***37**, 145-153 (2019).
- 16 Rubaltelli, L. *et al.* Contrast-enhanced ultrasound for characterizing lymph nodes with focal cortical thickening in patients with cutaneous melanoma. *AJR Am J Roentgeno***196**, W8-12 (2011).
- 17 Rubaltelli, L. *et al.* Automated quantitative evaluation of lymph node perfusion on contrast-enhanced sonography. *AJR Am J Roentgeno***188**, 977-983 (2007).
- 18 Morimoto, Y. *et al.* Correlation between the incidence of central nodal necrosis in cervical lymph node metastasis and the extent of differentiation in oral squamous cell carcinoma. *Dentomaxillofac Rad***35**, 18-23 (2006).
- 19 Miura, Y. *et al.* Early diagnosis of lymph node metastasis: Importance of intranodal pressures. *Cancer Sci***107**, 224-232 (2016).
- 20 Mikada, M. *et al.* Evaluation of the enhanced permeability and retention effect in the early stages of lymph node metastasis. *Cancer Sci***108**, 846-852 (2017).
- 21 Jeong, H. S. *et al.* Investigation of the Lack of Angiogenesis in the Formation of Lymph Node Metastases. *Journal of the National Cancer Institute***107**, djv155 (2015).
- 22 Kumar, V., Chyou, S., Stein, J. V. & Lu, T. T. Optical projection tomography reveals dynamics of HEV growth after immunization with protein plus CFA and features shared with HEVs in acute autoinflammatory lymphadenopathy. *Front Immunol***3**, 282 (2012).

- 23 Kelch, I. D. *et al.* Organ-wide 3D-imaging and topological analysis of the continuous microvascular network in a murine lymph node. *Sci Rep***5**, 16534 (2015).
- 24 Jafarnejad, M. *et al.* Quantification of the Whole Lymph Node Vasculature Based on Tomography of the Vessel Corrosion Casts. *Sci Rep***9**, 13380 (2019).
- 25 Iwamura, R., Sakamoto, M., Mori, S. & Kodama, T. Imaging of the Mouse Lymphatic Sinus during Early Stage Lymph Node Metastasis Using Intranodal Lymphangiography with X-ray Micro-computed Tomography. *Mol Imaging Biol***21**, 825-834 (2019).
- 26 Liu, G. *et al.* BI-RADS 4 breast lesions: could multi-mode ultrasound be helpful for their diagnosis? *Gland Surg***8**, 258-270 (2019).
- 27 Metz, S. *et al.* Detection and quantification of breast tumor necrosis with MR imaging: value of the necrosis-avid contrast agent Gadophrin-3. *Acad Radiol***10**, 484-490 (2003).
- 28 Petralia, G., Conte, G., Fiori, E. D., Alessi, S. & Bellomi, M. Contrast-enhanced ultrasound sonography optimises the assessment of lymph nodes in oncology. *Ecancermedicalscience***7**, 328 (2013).
- 29 Ecanow, J. S., Abe, H., Newstead, G. M., Ecanow, D. B. & Jeske, J. M. Axillary staging of breast cancer: what the radiologist should know. *Radiographics***33**, 1589-1612 (2013).
- 30 Dhawan, I. *et al.* Detection of cervical lymph node micrometastasis and isolated tumor cells in oral squamous cell carcinoma using immunohistochemistry and serial sectioning. *J Oral Maxillofac Pathol***20**, 436-444 (2016).
- 31 Yaghan, R. *et al.* Oestrogen receptor status predicts local recurrence following breast conservation surgery for early breast cancer. *Eur J Surg Oncol***24**, 424-426 (1998).
- 32 Lovekin, C. *et al.* c-erbB-2 oncoprotein expression in primary and advanced breast cancer. *Br J Cancer***63**, 439-443, doi:10.1038/bjc.1991.101 (1991).
- 33 Cabral, H. *et al.* Systemic Targeting of Lymph Node Metastasis through the Blood Vascular System by Using Size-Controlled Nanocarriers. *ACS nano***9**, 4957-4967 (2015).
- 34 Liu, J. *et al.* Enhanced Primary Tumor Penetration Facilitates Nanoparticle Draining into Lymph Nodes after Systemic Injection for Tumor Metastasis Inhibition. *ACS nano***13**, 8648-8658 (2019).
- 35 Tada, A., Horie, S., Mori, S. & Kodama, T. Therapeutic effect of cisplatin given with a lymphatic drug delivery system on false-negative metastatic lymph nodes. *Cancer Sci***108**, 2115-2121 (2017).
- 36 Fujii, H. *et al.* Treatment of false-negative metastatic lymph nodes by a lymphatic drug delivery system with 5-fluorouracil. *Cancer Med***8**, 2241-2251 (2019).

37 Percie du Sert, N. *et al.* Reporting animal research: Explanation and elaboration for the ARRIVE guidelines 2.0. *PLoS Bio***18**, e3000411 (2020).

38 Shao, L. *et al.* Lymphatic mapping of mice with systemic lymphoproliferative disorder: Usefulness as an inter-lymph node metastasis model of cancer. *J Immunol Methods***389**, 69-78 (2013).

39 Ito, K. *et al.* High-Accuracy Ultrasound Contrast Agent Detection Method for Diagnostic Ultrasound Imaging Systems. *Ultrasound Med Bio***41**, 3120-3130 (2015).

40 Kochi, T. *et al.* Characterization of the arterial anatomy of the murine hindlimb: functional role in the design and understanding of ischemia models. *PloS one***8**, e84047 (2013).

## Figures

Figure 1

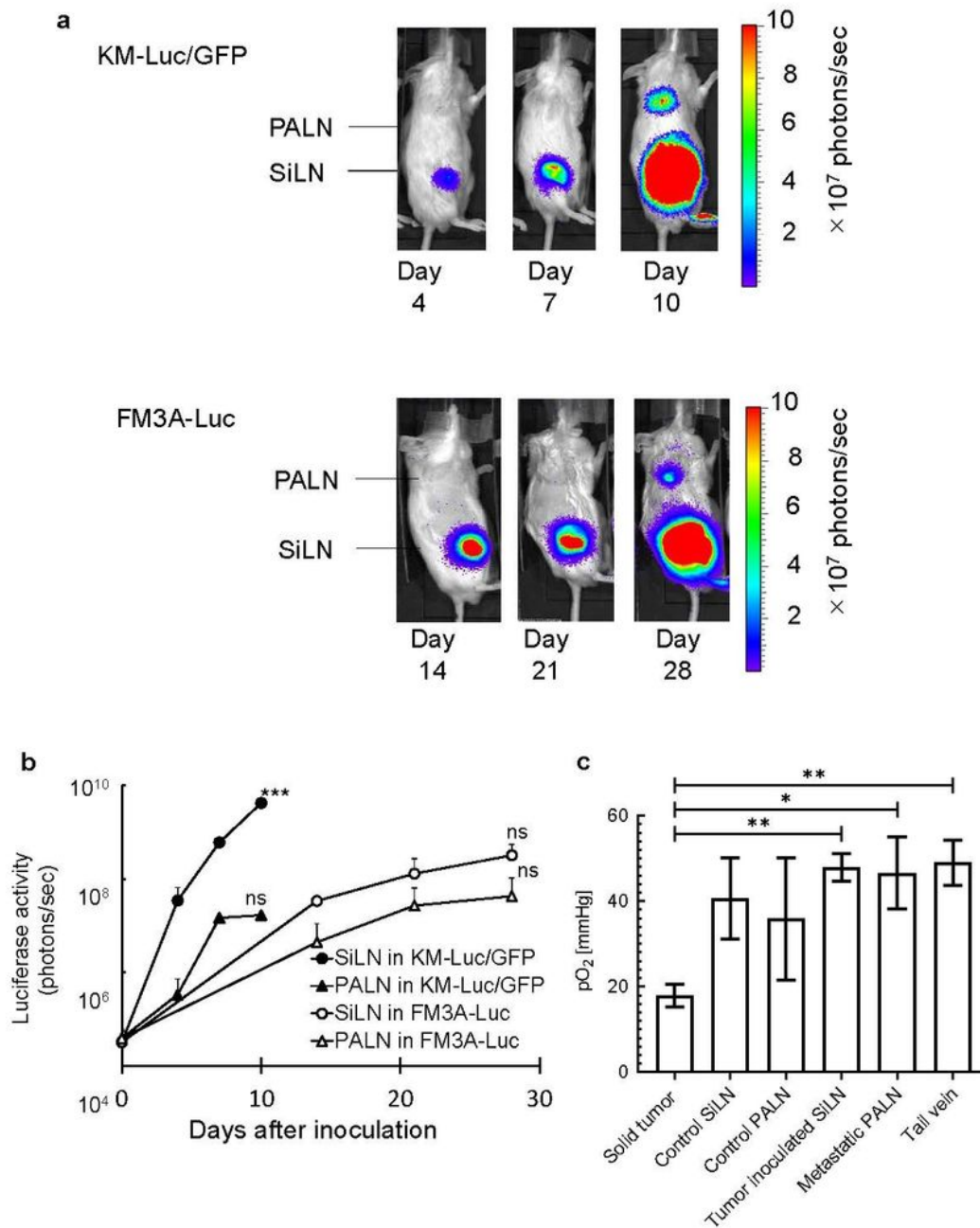


Figure 1

Progression of metastasis a, In vivo bioluminescence imaging. Tumor cells were injected into the SiLN to induce metastasis to the PALN. Metastasis was detected from day 7 for KM-Luc/GFP cells and from day 14 for FM3A-Luc cells. b, Graphical description of luciferase activity vs days after inoculation. KM-Luc/GFP cells: day 0 (n = 6), day 4 (n = 5), day 7 (n = 6) and day 10 (n = 5). FM3A-Luc cells: day 0 (n = 6), day 14 (n = 5), day 21 (n = 6) and day 28 (n = 5). Significant differences were found among the groups

(one-way ANOVA and Tukey's post-hoc test): SiLN, KM-Luc/GFP group, \*\*\*  $P < 0.001$ , day 0 vs day 10. Data are shown as mean  $\pm$  S.E.M. ns: not significant. c, pO<sub>2</sub> measurements made in the solid tumor (n = 2), control SiLN (n = 14), control PALN (n = 14), tumor-inoculated SiLN (n = 7), metastatic PALN (n = 7) and tail vein (n = 5). Significant differences were found among the groups (one-way ANOVA and Tukey's post-hoc test): \*  $P < 0.05$ , solid tumor vs metastatic PALN, \*\*  $P < 0.01$ , solid tumor vs tumor inoculated SiLN, and \*\*  $P < 0.01$ , solid tumor vs tail vein. Data are shown as mean  $\pm$  S.E.M.

Figure 2

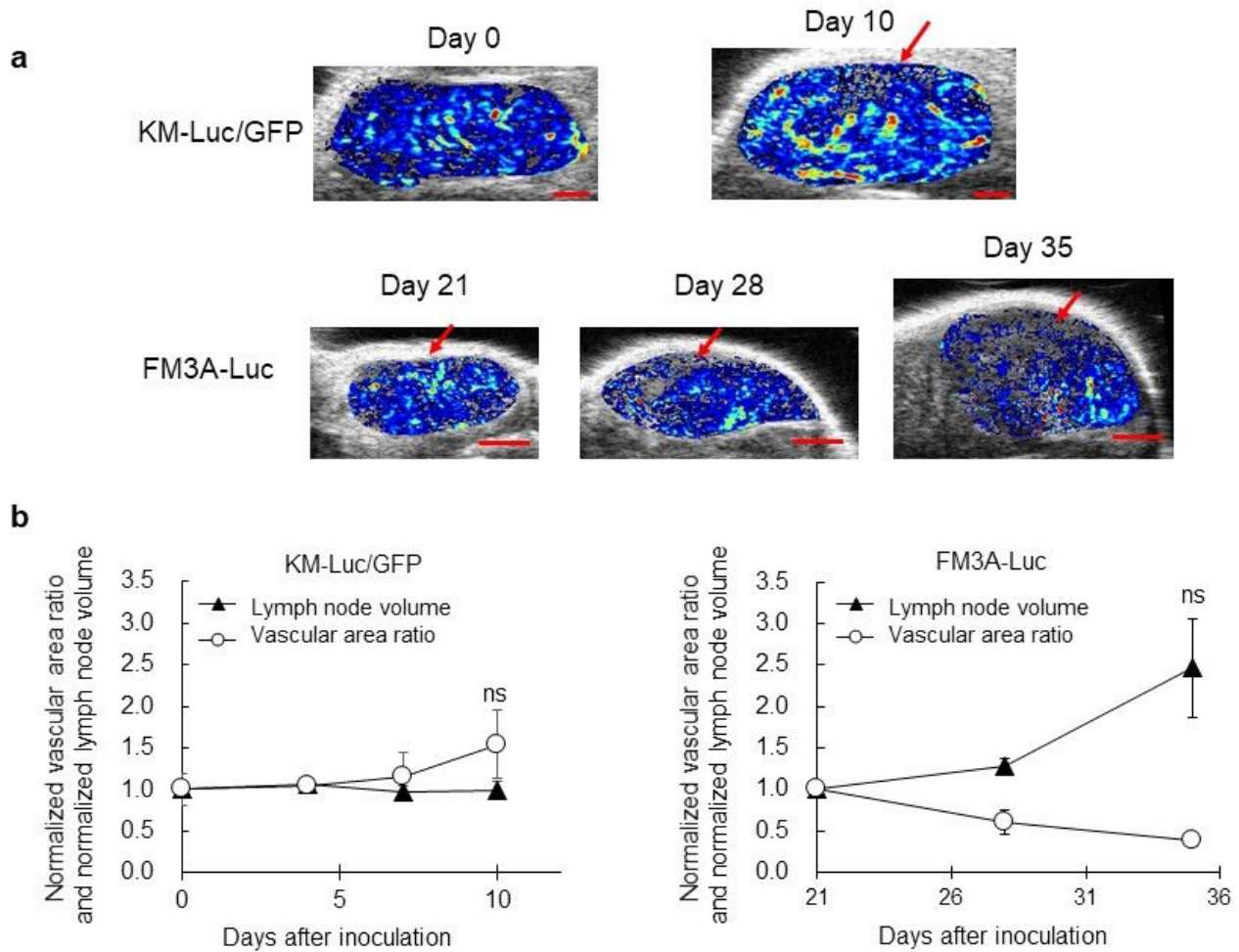


Figure 2

Contrast-enhanced high-frequency ultrasound imaging a, Representative heatmaps of the PALN on days 0 and 10 after inoculation of KM-Luc/GFP cells into the SiLN and on days 21, 28 and 35 after inoculation of FM3A-Luc cells. The heatmaps were generated from contrast-enhanced high-frequency ultrasound images using UCAD software. Arrows: perfusion defect. b, Changes in normalized vascular area ratio and normalized volume of the PALN. KM-Luc/GFP or FM3A-Luc cells were inoculated into the SiLN to induce metastasis to the PALN. KM-Luc/GFP cells: day 4 (n = 6), day 7 (n = 6) and day 10 (n = 6). FM3A-Luc cells: day 21 (n = 10), day 28 (n = 9) and day 35 (n = 10). There were no significant changes in

normalized LN volume or normalized vascular area ratio in the metastatic PALN (one-way ANOVA and Tukey's post-hoc test). Data are shown as mean  $\pm$  S.E.M. ns: not significant.

Figure 3

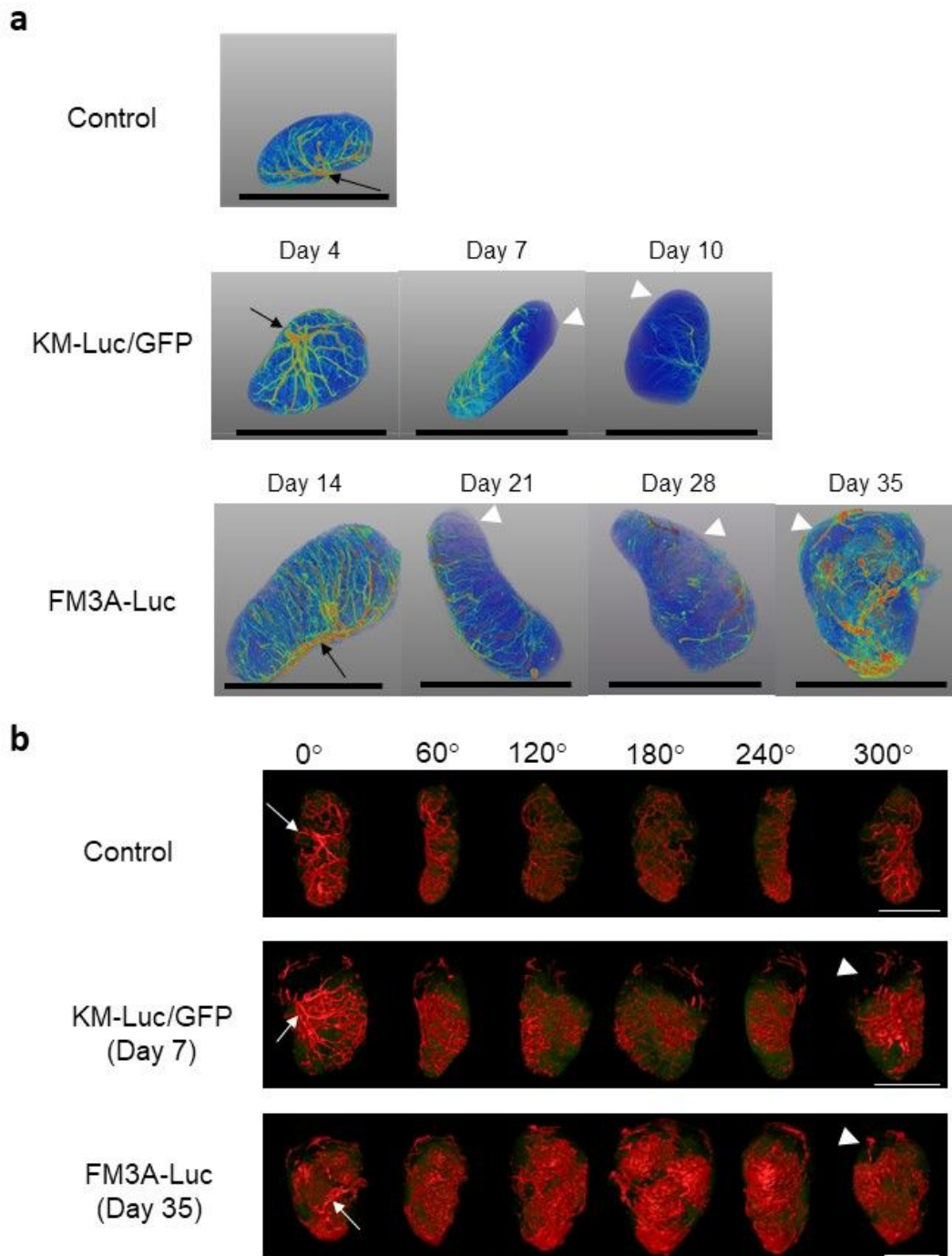


Figure 3

3D vascular structures in the PALN visualized by ex vivo contrast-enhanced micro-CT imaging a, 3D heatmaps. Images were captured at days 4, 7 and 10 for the KM-Luc/GFP group and days 14, 21, 28 and 35 for the FM3A-Luc group. Arrowheads: perfusion defect area. Arrows: TEV. Scale bar: 10 mm. b, 3D

images showing the surface and internal vascular structure of the PALN. The series of images shows the LN rotated by 60° each time. Arrowheads: perfusion defect area. Arrows: TEV. Spatial resolution: 8–30 μm. Scale bar: 5 mm.

Figure 4

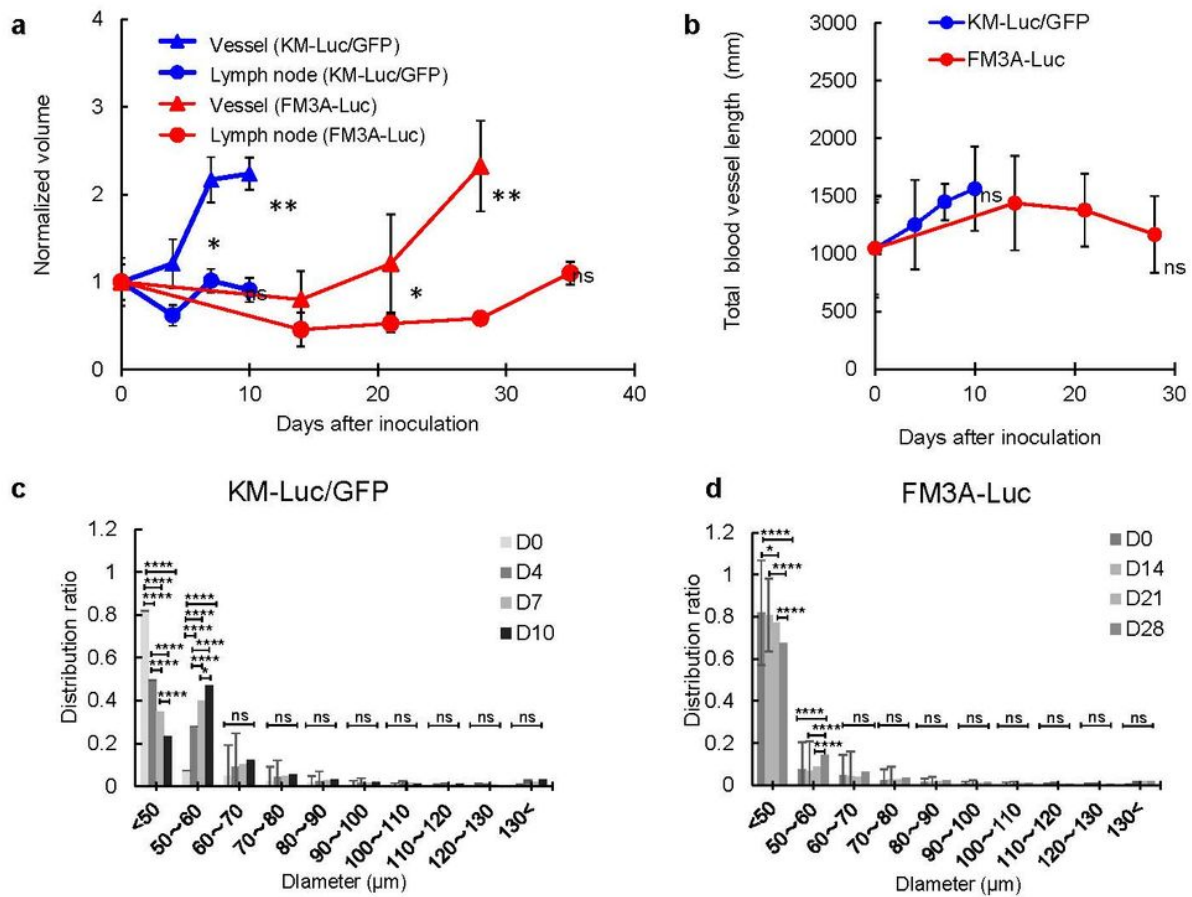
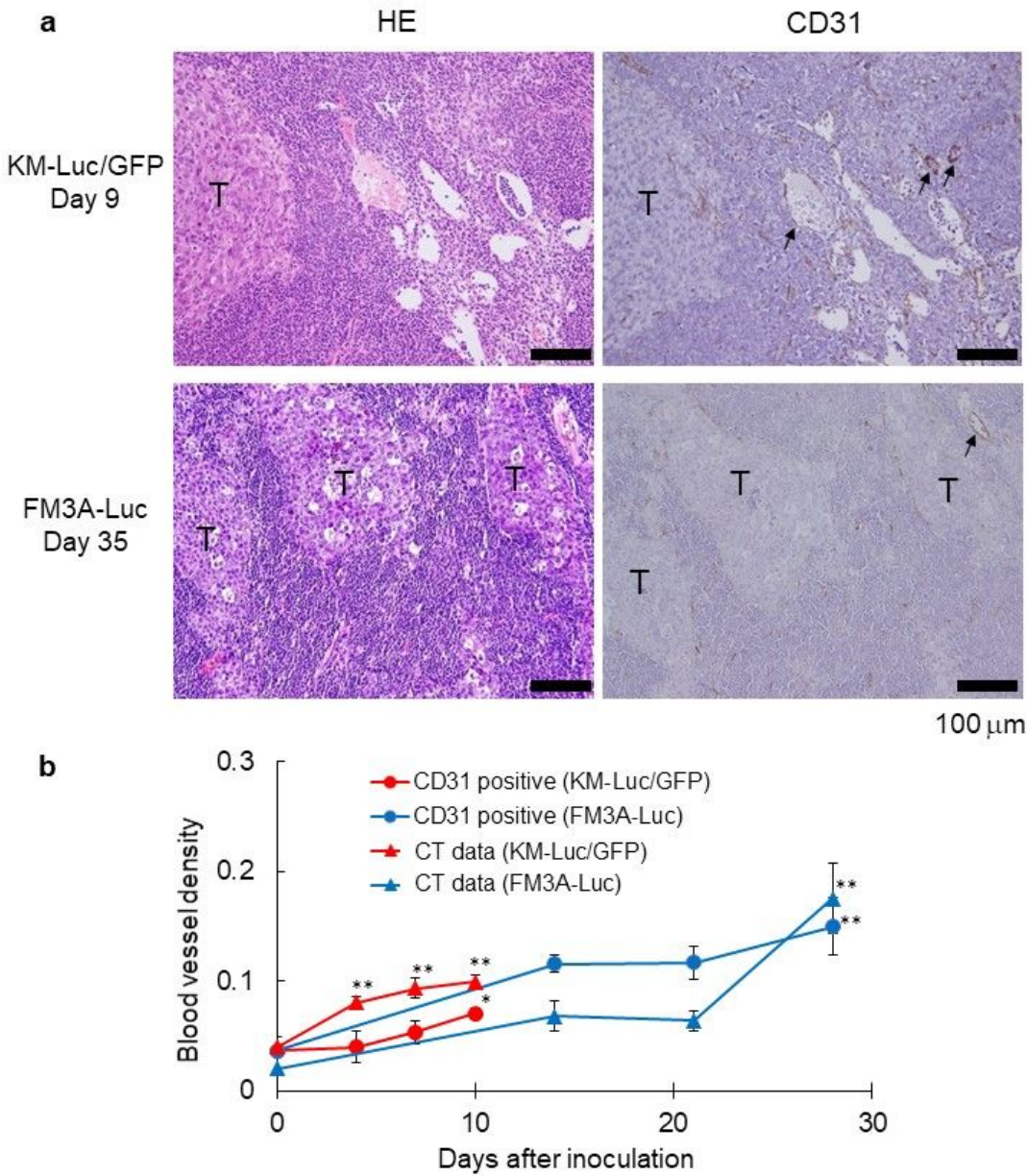


Figure 4

Characteristics of the blood vessels in the metastatic PALN KM-Luc/GFP cells or FM3A-Luc cells were inoculated into the SiLN to induce metastasis to the PALN. a, Changes in the normalized blood vessel volume and normalized LN size measured by contrast-enhanced micro-CT. Blood vessel volume for the KM-Luc/GFP group, one-way ANOVA, \*  $P < 0.05$ , day 0 vs day 7, \*\*  $P < 0.005$ , day 0 vs day 10; blood vessel volume for the FM3A-Luc group, one-way ANOVA, \*  $P < 0.05$ , day 0 vs day 21, \*\*  $P < 0.005$ , day 0 vs day 28. Data are shown as mean  $\pm$  S.E.M. b, Total blood vessel length measured by contrast-enhanced micro-CT. Data are shown as mean  $\pm$  S.E.M. There were no significant differences among the groups. ns: not significant. c, Distribution of blood vessel diameter in the PALN after the inoculation of KM-Luc/GFP cells. Blood vessels with a diameter  $< 50 \mu\text{m}$  accounted for more than 80% of blood vessels on day 0. The proportion of blood vessels with a diameter  $< 50 \mu\text{m}$  decreased with time, and the proportion of blood vessels with diameters in the range 50–60  $\mu\text{m}$  increased by more than 50%. KM-Luc/GFP cells: day 4 ( $n = 5$ ), day 7 ( $n = 6$ ) and day 10 ( $n = 5$ ). Blood vessel diameter distribution,  $< 50 \mu\text{m}$ , one-way ANOVA, \*\*\*\*  $P <$

0.000, day 0 vs day 4, \*\*\*\* P < 0.0001, day 0 vs day 7, \*\*\*\* P < 0.000, day 0 vs day 10, \*\* P < 0.005, day 4 vs day 7, \*\*\*\* P < 0.000, day 4 vs day 10, \* P < 0.05, day 7 vs day 10; 50–60  $\mu\text{m}$ , \*\*\*\* P < 0.000, day 0 vs day 4, \*\*\*\* P < 0.000, day 0 vs day 7, \* P < 0.05, day 0 vs day 10, \* P < 0.05, day 4 vs day 7, \*\*\* P < 0.001, day 4 vs day 10. Data are shown as mean  $\pm$  S.E.M. ns: not significant. d, Distribution of blood vessel diameter in the PALN following the inoculation of FM3A-Luc cells. Blood vessels with a diameter < 50  $\mu\text{m}$  accounted for more than 60% of all blood vessels on each day. FM3A-Luc cells: day 0 (n = 6), day 14 (n = 5), day 21 (n = 6) and day 28 (n = 5). Blood vessel diameter distribution, < 50  $\mu\text{m}$ , one-way ANOVA, \*\*\*\* P < 0.000, day 0 vs day 28, \*\* P < 0.01, day 14 vs day 21, \*\*\* P < 0.001, day 14 vs day 28, \*\* P < 0.01, day 21 vs day 28. Data are shown as mean  $\pm$  S.E.M. ns: not significant.

Figure 5



**Figure 5**

Histological evaluation of perfusion defects in PALNs a, Serial sections of metastatic PALNs on day 10 after inoculation of KM-Luc/GFP cells and day 35 after inoculation of FM3A-Luc cells into the SiLN. The sections were stained with HE or immunostained for CD31. KM-Luc/GFP cells formed a tumor mass in the LN and proliferated expansively, and the boundary with the surrounding normal tissue was quite well defined. There were no mature blood vessels containing blood in the tumor mass. There were blood

vessels around the tumor mass that appeared to be compressed, and some dilated blood vessels were also evident. FM3A-Luc cells proliferated invasively in the LN, and the boundary with surrounding normal tissue was poorly defined. No mature blood vessels containing blood were seen in the tumor tissue. Tumor cells had infiltrated the surrounding tissue's blood vessels to destroy the vasculature at the invasion site, and no dilated blood vessels were found in the tissue surrounding the tumor. Scale bar: 100  $\mu\text{m}$ . Arrows, CD31-positive endothelial cells; T, tumor. b. Blood vessel density calculated from images immunostained for CD31. Blood vessel density, CD31 immunostaining data, one-way ANOVA: KM-Luc/GFP group, \*  $P < 0.05$ , day 0 vs day 10; FM3A-Luc group, \*\*  $P < 0.01$ , day 0 vs day 28. Blood vessel density, CT data: KM-Luc/GFP group, \*\*  $P < 0.01$ , day 0 vs day 4, \*\*  $P < 0.01$ , day 0 vs day 7, \*\*  $P < 0.01$ , day 0 vs day 10; FM3A-Luc group, \*\*  $P < 0.01$ , day 0 vs day 28. Data are shown as mean  $\pm$  S.E.M.

## Supplementary Files

This is a list of supplementary files associated with this preprint. Click to download.

- [SupplementaryVideo1Control.avi](#)
- [SupplementaryVideo2KMLucGFPday7.avi](#)
- [SupplementaryVideo3FM3Aday35.avi](#)
- [SupplementaryinformationSciRep20210120final.docx](#)